

Detailed studies of IPHAS sources - I. The disrupted late bipolar IPHASX J193718.6+202102

L. Sabin^{1*}, M.A. Guerrero², S. Zavala³, J.A. Toalá⁴, G. Ramos-Larios⁵ and V. Gómez-Llanos¹

¹*Instituto de Astronomía, Universidad Nacional Autónoma de México, Apdo. Postal 877, 22800 Ensenada, B.C., Mexico*

²*Instituto de Astrofísica de Andalucía (IAA-CSIC), Glorieta de la Astronomía S/N, 18008 Granada, Spain*

³*Tecnológico Nacional de México / I. T. Ensenada (TecNM/ITE), Blvd. Tecnológico No. 150, C. P. 22780, Ensenada, B. C., Mexico*

⁴*Instituto de Radioastronomía y Astrofísica (IRyA), UNAM Campus Morelia, Apartado postal 3-72, 58090 Morelia, Michoacan, Mexico*

⁵*Instituto de Astronomía y Meteorología, Universidad de Guadalajara, Av. Vallarta 2602, Arcos Vallarta, 44130 Guadalajara, Mexico*

24 February 2022

ABSTRACT

We present a detailed analysis of the new planetary nebula (PN) IPHASX J193718.6+202102 using deep imaging and intermediate- and high resolution spectroscopy that are interpreted through morpho-kinematic and photoionisation modelling. The physical structure of the nebula consists of a fragmented torus and an extremely faint orthogonal bipolar outflow, contrary to the pinched waist PN morphology suggested by its optical image. Our kinematic analysis indicates that the torus is expanding at $25 \pm 5 \text{ km s}^{-1}$ and is gradually breaking up. At an estimated distance of $7.1^{+0.8}_{-0.3} \text{ kpc}$, the corresponding kinematic age of ~ 26000 years is consistent with a faint and disintegrating PN. The intermediate-resolution spectra reveal an excited PN with chemical abundances typical of Type II PNe. Based on the latter we also estimate an initial mass for the progenitor in the range $2\text{--}3 M_{\odot}$ and a central star (CSPN) mass $M_{\text{CSPN}} \sim 0.61 M_{\odot}$. The *Spitzer* MIPS $24 \mu\text{m}$ emission that closely follows the fragmented torus could be attributed to the emission of [O IV] at $25.9 \mu\text{m}$ rather than to dust emission. All the results coherently point towards an evolved moderately massive bipolar Type II PN on the brink of dissolving into the interstellar medium.

Key words: ISM: kinematics and dynamics; ISM: abundances; planetary nebulae: individual: IPHASX J193718.6+202102

1 INTRODUCTION

The Isaac Newton Telescope (INT) Photometric H α survey (IPHAS; Drew et al. 2005; González-Solares et al. 2008; Barentsen et al. 2014) was designed to provide a more complete sampling of the stellar population in the Northern Galactic Plane between $\pm 5^{\circ}$. In particular, the survey has allowed the discovery of hundreds of new planetary nebulae (PNe), most of which either present a low surface brightness, which hampered their earlier detection, or were too compact to be clearly identified towards this crowded region of the Galactic Plane.

These nebulae, which are ionized by the radiation field of evolved intermediate-mass stars, can be used to probe stellar mass loss and Galactic chemical evolution for example. IPHAS is an excellent tool to study very compact PNe (which can be young and/or distant; Viironen et al. 2009; Akas et al. 2019) as well as extended faint (and likely evolved) PNe (Sabin et al. 2014). One of the most striking aspects of PNe is their morphology (Balick & Frank 2002; Sahai et al. 2011). Indeed, most of them depart from spherical symmetry and the reason(s) for such behaviour has led to important progresses in research fields such as the study of binary systems (Hillwig et al. 2016; Jones & Boffin 2017) and magnetic fields (Asensio Ramos et al. 2014; Tocknell et al. 2014). Advances were also made with kine-

matic studies and modelling (López et al. 2012; Sabin et al. 2017; García-Díaz et al. 2018), chemical analyses (Corradi et al. 2015; Jones et al. 2016; Wesson et al. 2018) and (magneto)hydrodynamics modelling (Huarte-Espinosa et al. 2012; Balick et al. 2018). These tools can be used to investigate the characteristics of the newly discovered IPHAS PNe which can differ from those of the generally brighter known PNe, hence providing a more global view of the PN population in the Galactic Plane. We therefore initiate here a series of publications dedicated to detailed analyses of individual IPHAS low surface brightness sources and PNe in particular.

In this article we present the case of the PN IPHASX J193718.6+202102 (PN G056.1–00.4). This object is included in the catalogue of Sabin et al. (2014) as a true PN, with the number 99 in its table 3, based on a follow up identification spectrum obtained at the Isaac Newton telescope (INT, La Palma). Accordingly, we will refer to it as Sab 99 afterwards.

The IPHAS images could only provide limited information on its morphology due to the short 120 seconds exposure in the wide H α filter, but they hint at a peculiar morphology. The nebula presents two parallel string-like features with discontinued emission resembling a set of knots. Such morphology led us to propose a classification as a bipolar PN with multiple shells or external structures and resolved internal structures (“Bas”, according to the classification scheme by Sabin et al. 2014).

In the following we present a more detailed analysis of Sab 99

* E-mail: lsabin@astro.unam.mx

using new deeper observations. Imaging, intermediate- and high-dispersion spectroscopic observations are described in section §2. The results of each method are shown in §3. An infrared analysis based on *Spitzer* data is also presented in section §4. All the data will be used to establish a morpho-kinematic model to help us understand the evolutionary status of this PN (§5). Our discussion and concluding remarks are presented in §6 and §7, respectively.

2 OBSERVATIONS

2.1 NOT ALFOSC imaging

Sab 99 was observed with the Alhambra Faint Object Spectrograph and Camera (ALFOSC) mounted on the 2.5 m Nordic Optical Telescope (NOT) at the Observatorio Roque de los Muchachos (ORM, La Palma, Spain). The camera is equipped with a 2048×2048 EEV CCD ($13.5 \mu\text{m}$ pixel size) detector providing a plate scale of $0''.184 \text{ pix}^{-1}$ and a field of view of $6'.3 \times 6'.3$. Three sets of narrow-band images with exposure times 3×600 s were obtained on 2016 November 27 using the $\text{H}\alpha$ ($\lambda_c = 6567 \text{ \AA}$, $\text{FWHM} = 8 \text{ \AA}$), $[\text{N II}]$ ($\lambda_c = 6588 \text{ \AA}$, $\text{FWHM} = 9 \text{ \AA}$), and $[\text{O III}]$ ($\lambda_c = 5007 \text{ \AA}$, $\text{FWHM} = 30 \text{ \AA}$) filters. The observing conditions were excellent with a seeing between $0''.6$ and $0''.8$ based on the FWHM of stars in the field. All the images were reduced using standard IRAF¹ routines (Tody 1986). The individual narrow-band images and a color-composite picture are presented in Figure 1.

2.2 MES high resolution spectroscopy

Long-slit high dispersion optical spectra of Sab 99 were acquired with the Manchester Echelle Spectrograph (MES, Meaburn et al. 2003) installed on the 2.12 m telescope at the Observatorio Astronómico Nacional, San Pedro Mártir (OAN-SPM, Mexico). The detector used was a 2048×2048 pixels E2V CCD with a pixel size of $13.5 \mu\text{m}$. The slit length was $6'.5$ and the slit width was $150 \mu\text{m}$ corresponding to $1''.9$. The observations were obtained with 2×2 and 4×4 binning, resulting in spatial scales and spectral dispersions of $0''.351 \text{ pix}^{-1}$ and $0.05 \text{ \AA pix}^{-1}$, and $0''.702 \text{ pix}^{-1}$ and 0.1 \AA pix^{-1} , respectively. An $\text{H}\alpha$ filter with $\Delta\lambda = 90 \text{ \AA}$ was used to isolate the 87th echelle order including the $\text{H}\alpha$ and the $[\text{N II}] \lambda\lambda 6548, 6584$ lines. Eight 1800s spectra were obtained with the slits placed across different nebular features to provide a complete map the velocity field of Sab 99. Table 1 summarizes the different observations realized with MES and the position of each slit is shown in Figure 2. A ThAr lamp was used for wavelength calibration and the data were reduced using standard IRAF packages.

The FWHM of the arc lamp emission lines indicate a spectral resolution $\sim 12 \text{ km s}^{-1}$.

2.3 GTC OSIRIS intermediate resolution spectroscopy

Intermediate resolution spectroscopy was performed with the 10.4 m Gran Telescopio Canarias (GTC) and the Optical System for Imaging and low-Intermediate-Resolution Integrated Spectroscopy OSIRIS at ORM (La Palma, Spain). Two Marconi CCD42-82 (2048×4096 pixels) detectors were used and a 2×2 binning was

Table 1. MES Observing log

Slit	Observation Date	PA ($^\circ$)	Binning pixels	Seeing ($''$)
A	2017/08/05	−65	2×2	1.4
B	2018/05/27	−65	2×2	1.2
C	2018/05/27	−65	4×4	1.3
D	2017/08/06	−65	2×2	1.3
E	2017/08/06	−65	2×2	1.2
F	2018/05/28	−10	2×2	1.3
G	2018/05/27	−10	2×2	1.2
H	2017/08/06	−10	2×2	1.4

Table 2. GTC Observing log

Slit	Observation Date	PA ($^\circ$)	Seeing ($''$)
a	2018/05/22	−65	1.0
b	2018/06/04	−78	0.8
c	2017/08/19	−10	1.3

employed, leading to a spatial scale of $0''.254 \text{ pix}^{-1}$. The R1000B grism was used, providing a spectral coverage $3630\text{--}7500 \text{ \AA}$ and a dispersion of $2.12 \text{ \AA pix}^{-1}$. In order to obtain a good coverage of the nebula, spectra were obtained for three slit positions across morphological features of interest (see Tab. 2 and Fig. 2). In all cases the slit length was $7'.4$ and the slit width $0''.8$, leading to a spectral resolution of 6.15 \AA .

The exposure time was $3 \times 1200 \text{ s}$ for each slit. The wavelength calibration was performed with HgAr and Ne lamps and the flux calibration was achieved with the standard stars GD140, GD190 and Feige 110. The data reduction was carried out using standard IRAF routines.

2.4 OSN broad band imaging

Broadband U , B , V and R images were obtained on 2019 November 7 with the 1.5m telescope located at the Sierra Nevada observatory (OSN, Spain) as part of a Director Discretionary Time program. We used the 2048×2048 pixels CCDT150 camera with a pixel size of $13.5 \mu\text{m}$, resulting in a plate scale of $0''.232 \text{ pix}^{-1}$ and a field of view of $7'.92 \times 7'.92$. A 2×2 binning factor was employed. In total, we obtained 6 exposures of 100s in each filter except the U filter where we used 6 exposures of 600s. The photometric calibration was performed with the Landolt fields G26-7 and G93-48.

2.5 Spitzer MIPS imaging

We used the NASA/IPAC Infrared Science Archive (IRSA) and retrieved *Spitzer*/MIPS (Multiband Imaging Photometer for *Spitzer*, Rieke et al. 2004) data from the MIPS Galactic Plane legacy survey MIPS GAL². MIPS, which has a $128 \times 128 \text{ Si:As}$ detector and a $24 \mu\text{m}$ pixel size, provides image and photometric data in the bands centered at 24, 70, and $160 \mu\text{m}$ with spatial resolution of $6''.0$, $18''.0$, and $40''.0$, respectively.

¹ IRAF is distributed by the National Optical Astronomy Observatories, which is operated by the Association of Universities for Research in Astronomy, Inc. (AURA) under cooperative agreement with the National Science Foundation.

² <https://irsa.ipac.caltech.edu/data/SPITZER/MIPSGAL/>

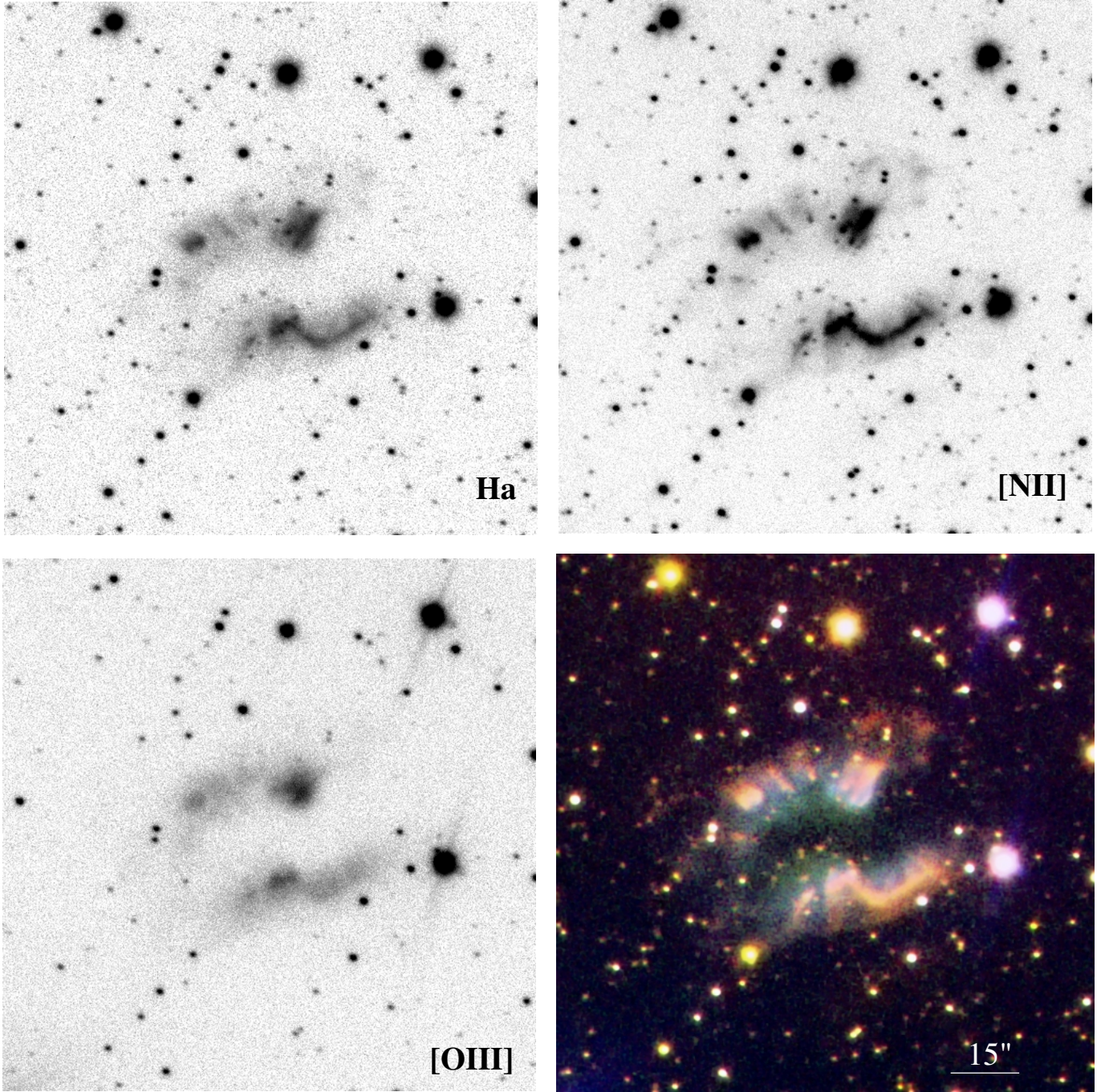


Figure 1. NOT ALFOSC narrow-band images of Sab 99 and color composite picture with [N II] in red, $H\alpha$ in green, and [O III] in blue. North is up, East to the left.

3 ANALYSIS

3.1 Morphology

The high quality NOT imagery presented in Figure 1 reveals with great detail the morphology of Sab 99. The brightest components of Sab 99 are two $\sim 1'.0 \times 0'.7$ filamentary string-like features that mirror each other's curvature. They present a fragmented morphology, which is best seen in the [N II] light, where bright knots are followed by tails reminiscent of ionization shadows. Other PNe such as the

faint K 1-10 (Corradi & Schwarz 1995), PN G321.6+02.2 (Corradi et al. 1997), and the bright NGC 2818 (Vázquez 2012) show similar symmetric rims. In those cases these opposite symmetric arms draw the walls and waist of bipolar outflows.

The NOT images do not reveal any nebulosity surrounding the main bright central structure. It was not possible neither to identify a central star (CS) based on the UV-Excess Survey of the Northern Galactic Plane (UVEX, Groot et al. 2009). The observations ob-

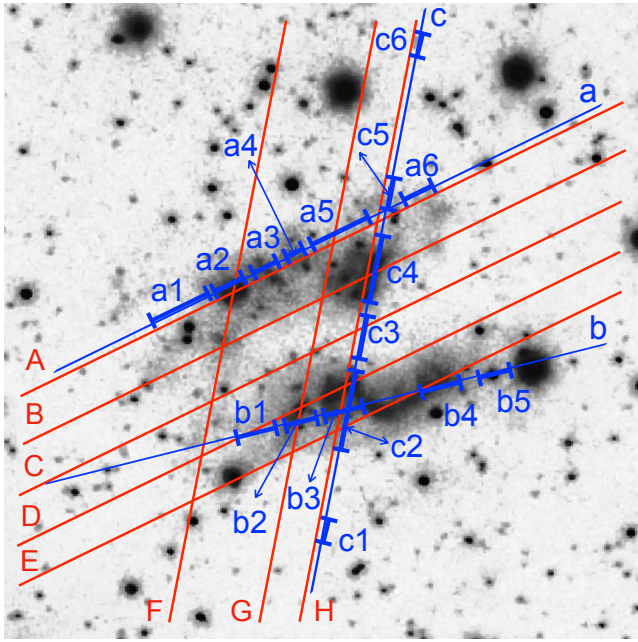


Figure 2. MES (red, upper-case letters) and GTC OSIRIS (blue, lower-case letters) slit positions superimposed on an image of Sab 99. The GTC OSIRIS slits *a* and *c* are spatially coincident with the MES slits A and H, respectively, but were displaced for clarity. The regions of the GTC OSIRIS spectra used for chemical analysis are labelled on the image as a1–a6, b1–b5, and c1–c6.

tained at the OSN did not detect a clear central star up to a limiting magnitude of 20 mag in the RGO *U* filter of UVEX.

3.2 Kinematics

The eight position-velocity (PV) diagrams shown in Figure 3 give a relatively complete view of the velocity field distribution in Sab 99. Slits A, B, D and E, going across the opposite arms (see their location in Fig. 2), underline the fragmented nature of the [N II] $\lambda 6583$ Å emission. The emission observed in these PV diagrams seems to show a faint curved expansion below and above the bright central region. However, these patterns are not an indication for the presence of additional emission from an extended outflow along the slit, as the full extent $\sim 50''$ of the [N II] emission in these diagrams is consistent with the size of the nebula in the narrow-band images in Figure 1. The H α emission is concentrated in the center of the nebula as shown by the slit C and tends to show some curvature.

Since it was not possible to derive the systemic velocity of the PN due to its morphology and the impossibility to precisely locate the central star, the radial velocities of individual features in the [N II] PV diagrams in Table 3 are only corrected from the Local Standard of Rest. The distribution of these velocities is illustrated in Figure 4, with peak values ranging from $+30.2$ km s $^{-1}$ to -27.8 km s $^{-1}$. Apart from some outliers, a general trend can be observed with the upper arm being blue-shifted, while the lower one is red-shifted. The velocity distribution of both structures is not symmetric though, but we note that the FWHM for each data point is quite large, with a mean of 20.8 km s $^{-1}$.

We also note that the velocity variations found among adjacent knots, such as the knots I, J and K sampled by Slit B, are indicative of the loose spatio-kinematic structure of the torus (see Section 6).

Table 3. Radial velocities (in the LSR) and FWHM of bright features covered by slits A, B, D, and E. Each feature can spatially be identified on Figure 4.

Feature	Velocity (km s $^{-1}$)	FWHM (km s $^{-1}$)	Feature	Velocity (km s $^{-1}$)	FWHM (km s $^{-1}$)
A	+0.7	20	L	−4.0	20
B	−10.8	25	M	+9.5	37
C	−15.4	25	N	+7.9	14
D	−10.7	25	O	+15.4	19
E	−6.1	22	P	+16.1	23
F	−13.2	14	Q	+30.1	13
G	+5.7	18	R	+24.7	20
H	+2.4	23	S	+28.2	22
I	−27.8	19	T	+28.2	17
J	−6.7	24	U	+24.2	20
K	−9.6	18	V	+26.0	21

3.3 Chemistry

The chemical analysis of Sab 99 was performed with the GTC OSIRIS data at three position angles going along both strings of knots (PA = -65° and -78°) and across them (PA = -10°), as illustrated in Fig. 2.

One-dimensional spectra were extracted with the IRAF task *apall* from 17 different regions to map the chemistry across the nebula³. The PA on the sky of slits *a* and *b* were close to the parallactic angle, but that of slit *c* was mostly orthogonal, $\simeq 80^\circ$. At the airmass of the latter observation, $\simeq 1.2$, the differential chromatic diffraction between the most extremes [Ne III] $\lambda 3869$ Å and [Ar III] $\lambda 7751$ Å emission lines can amount up to $0''.8$, but it is $\leq 0''.4$ for the most important lines in the range 4800–6800 Å (Filippenko 1982). The slit width of $0''.8$ is just twice that value, but the diffuse nature of this source, with knots much more extended than the slit width and differential chromatic diffraction shift, minimizes the impact of the latter. This is further diluted by the use of aperture sizes significantly larger than the maximum value of the differential chromatic diffraction. The line fluxes were determined with the IRAF task *splot* and the errors associated to each intensity takes into account the statistical error (noise around the position of the corresponding line) and the errors due to the flux calibration. The data analysis was performed using the code PYNEB by Luridiana et al. (2015) and the data were corrected from extinction using the Cardelli et al. (1989) law with $R_V = 3.1$. Uncertainties in the physical conditions and ionic abundances determined by PYNEB were estimated using a Monte Carlo simulation of 1000 random values with a normal distribution around the observed intensity and a standard deviation (σ) of each line. The results of the analysis are shown in Tables 4, 5, and 6. We emphasize that we excluded throughout this analysis all measurements with errors greater than 50% (which roughly corresponds to a signal to noise ratio lower than 3). As a consequence, some regions are not included in the aforementioned tables due to the large errors or absence of the Balmer lines.

Sab 99 is characterised by a relatively large extinction and we derived mean logarithmic extinctions using the Cardelli et al. (1989) extinction law of $\langle c(H\beta) \rangle = 2.47 \pm 0.23$ along the upper arm (slit *a*), $\langle c(H\beta) \rangle = 2.59 \pm 0.18$ along the lower arm (slit *b*), and $\langle c(H\beta) \rangle = 2.56 \pm 0.12$ for the transverse region (slit *c*). The values are relatively

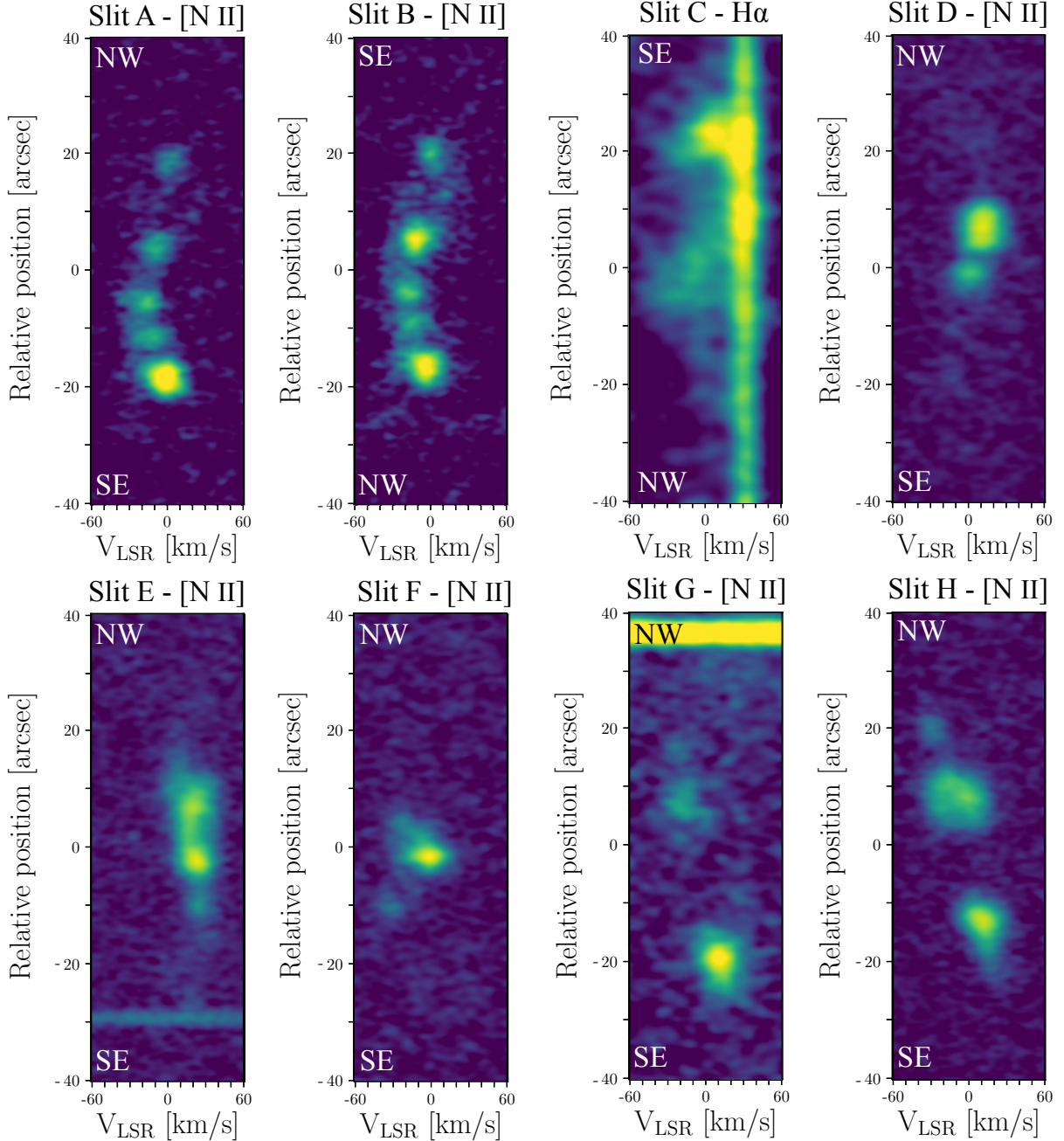


Figure 3. MES PV diagrams of the [N II] $\lambda 6583$ Å emission line, except for slit C, which shows the H α emission line. The bright line in the PV diagram of slit C at velocity ~ 30 km s $^{-1}$ is a telluric line, which was not removed to avoid affecting the spectrum. All the images were Gaussian smoothed to enhance faint structures.

consistent with each other and lead to a mean $c(H\beta)$ of 2.54 ± 0.18 for the whole nebula.

It was possible to derive the electronic temperatures and corresponding densities in the brightest a2, b3, b4 and c4 regions due to the presence of the [N II] 5755 Å line and sulfur doublet [S II] 6716, 6731 Å. The mean values obtained from the Monte Carlo distribution, as well as the associated standard deviations, are shown in Table 7. The mean T_e [N II] and n_e [S II] over the whole nebula are ~ 9600 K and ~ 380 cm $^{-3}$, respectively. The uncertainty

or standard deviation on the density distribution is relatively large (especially in the region a2), but we note that the values derived in different areas are generally consistent. The He II $\lambda 4686$ Å emission line is detected with an He II to H β ratio ranging from 0.37 ± 0.04 to 0.97 ± 0.21 , with a mean value of 0.61 ± 0.04 that indicates a relatively excited nebula. The mean ionic and total abundances obtained for regions where values of T_e and n_e could be derived are presented in Table 8. For this purpose the PYNEB atomic data and Delgado-Inglada et al. (2014)’s ionic correction factors (ICFs) were

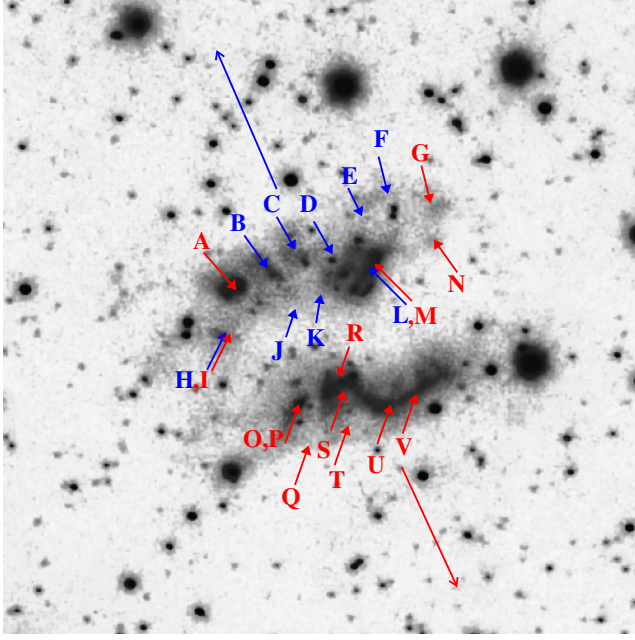


Figure 4. Spatial distribution on the different knots in Sab 99 for which their radial velocities have been measured (see Table 3). The blue arrows and letters illustrate the generally blue-shifted motion of the Northern arm and the red arrows and letters the global red-shifted motion of the Southern arm.

Table 4. Intrinsic intensities of emission lines in regions of the upper arm.

Ion	λ_0	a2	a3	a4	a5
H γ	4340	75 \pm 23
HeII	4686	39 \pm 7	53 \pm 14	49 \pm 11	...
H β	4861	100 \pm 12	100 \pm 17	100 \pm 18	100 \pm 38
[O III]	4959	447 \pm 45	435 \pm 60	463 \pm 67	626 \pm 175
[O III]	5007	1306 \pm 129	1432 \pm 191	1423 \pm 199	1714 \pm 478
[N I]	5199	9 \pm 3
[N II]	5755	7 \pm 2
HeI	5876	15 \pm 3	9 \pm 3
[O I]	6300	35 \pm 5	15 \pm 3	8 \pm 2	...
[O I]	6363	8 \pm 1
[N II]	6548	183 \pm 25	88 \pm 17	68 \pm 13	63 \pm 25
H α	6563	287 \pm 39	287 \pm 53	287 \pm 56	287 \pm 112
[N II]	6583	541 \pm 74	267 \pm 50	219 \pm 43	208 \pm 82
HeI	6678	3.4 \pm 0.7	2.8 \pm 1.2
[S II]	6716	50 \pm 7	38 \pm 8	36 \pm 8	36 \pm 15
[S II]	6731	39 \pm 6	27 \pm 5	26 \pm 6	23 \pm 10
HeI	7065	2.6 \pm 0.5	...	2.3 \pm 0.9	...
[Ar III]	7136	29 \pm 5	30 \pm 7	30 \pm 7	30 \pm 14
[O II]	7320	5.5 \pm 0.9	...	6 \pm 2	...
[O II]	7330	3.8 \pm 0.7
[Ar III]	7751	4.9 \pm 0.9	7 \pm 2	5 \pm 1	...
c(H β)		2.40 \pm 0.14	2.43 \pm 0.19	2.40 \pm 0.20	2.63 \pm 0.40

used.

The emission detected in the GTC slits a and b extends 58''4 and 48''5, respectively, i.e., no emission beyond the extent of the nebula disclosed in the narrow-band images is detected (see Fig. 1). However, a careful background subtraction of the GTC slit c unveils the presence of two faint [N II] blobs, one located 20''3 south from

Table 5. Intrinsic intensities of emission lines in regions of the lower arm.

Ion	λ_0	b2	b3	b4	b5
HeII	4686	105 \pm 25	72 \pm 11	67 \pm 10	...
H β	4861	100 \pm 21	100 \pm 13	100 \pm 14	100 \pm 16
[O III]	4959	447 \pm 74	405 \pm 44	395 \pm 47	511 \pm 68
[O III]	5007	1400 \pm 226	1189 \pm 127	1194 \pm 137	1481 \pm 193
[N II]	5755	...	4.0 \pm 0.9	6 \pm 1	...
HeI	5876	...	6 \pm 1	7 \pm 1	...
[O I]	6300	18 \pm 5	22 \pm 3	20 \pm 3	29 \pm 5
[O I]	6363	8 \pm 3	8 \pm 1	5.3 \pm 1.3	7 \pm 1
[N II]	6548	58 \pm 13	113 \pm 17	101 \pm 16	128 \pm 23
H α	6563	287 \pm 65	288 \pm 43	286 \pm 46	287 \pm 52
[N II]	6583	185 \pm 42	345 \pm 51	319 \pm 51	390 \pm 71
HeI	6678	2.7 \pm 1.2	3 \pm 1	2.8 \pm 0.7	5 \pm 2
[S II]	6716	26 \pm 6	40 \pm 6	36 \pm 6	33 \pm 7
[S II]	6731	22 \pm 5	35 \pm 5	29 \pm 5	23 \pm 5
HeI	7065	1.6 \pm 0.4	...
[Ar III]	7136	29 \pm 8	33 \pm 6	33 \pm 6	33 \pm 7
[O II]	7320	...	6 \pm 1	4.5 \pm 1.2	...
[O II]	7330	...	3.1 \pm 0.7	3.7 \pm 0.8	...
[Ar III]	7751	3.2 \pm 1.0	3 \pm 1	3.4 \pm 0.7	...
c(H β)		2.64 \pm 0.23	2.49 \pm 0.15	2.42 \pm 0.17	2.81 \pm 0.19

Table 6. Extracted regions with dereddened (I/H β) fluxes across the PN or Slit c

Ion	λ_0	c2	c4
[Ne III]	3869	...	217 \pm 55
[Ne III]	3968	...	110 \pm 31
H γ	4340	62 \pm 17	77 \pm 14
HeII	4686	72 \pm 8	66 \pm 6
H β	4861	100 \pm 10	100 \pm 9
[O III]	4959	418 \pm 38	499 \pm 42
[O III]	5007	1251 \pm 111	1464 \pm 123
HeI	5411	5 \pm 1	2.6 \pm 0.6
[N II]	5755	...	2.7 \pm 0.5
HeI	5876	...	11 \pm 1
[O I]	6300	17 \pm 2	10 \pm 1
[S III]+HeII	6312	...	3.3 \pm 0.4
[O I]	6363	4.5 \pm 0.7	3.2 \pm 0.4
[N II]	6548	97 \pm 12	86 \pm 10
H α	6563	287 \pm 36	290 \pm 34
[N II]	6583	313 \pm 39	261 \pm 31
HeI	6678	2.1 \pm 0.6	3.2 \pm 0.6
[S II]	6716	39 \pm 5	35 \pm 4
[S II]	6731	33 \pm 5	30 \pm 4
HeI	7065	2.1 \pm 0.5	2.1 \pm 0.4
[Ar III]	7136	30 \pm 4	33 \pm 4
[O II]	7320	...	4.0 \pm 0.8
[O II]	7330	...	2.0 \pm 0.3
[Ar III]	7751	4.4 \pm 0.8	5 \pm 1
c(H β)		2.58 \pm 0.13	2.55 \pm 0.12

position c2 and noted c1 in Figure 2, and another one at 42''4 north from position c4 and noted c6 in this same figure (see also Fig. 5–bottom panel). These emissions suggest the presence of the relics of an external structure along a direction orthogonal to that of the main nebula (see below).

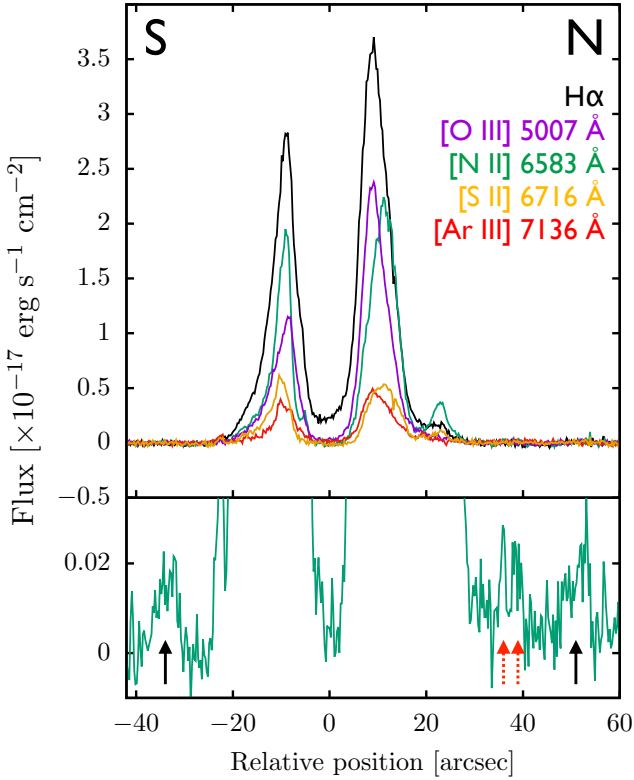


Figure 5. Spatial profiles of various emission lines in Sab 99 obtained through the GTC OSIRIS slit c. S and N show the southern and northern directions, respectively. The bottom panel presents a zoom of the [N II] profile to show the position of the clumps c1 and c6 (see Figure 2) marked with black solid black arrows (the red dashed-line arrows mark the location of the continuum emission from background stars).

Figure 5 shows the spatial profiles of various emission lines across slit c. It is worth highlighting the asymmetry in terms of fluxes, with H α , [O III], and [N II] emissions being brighter in the northern arm than in the southern one. The flux difference is less noticeable for [S II] and [Ar III]. Note also that the high excitation lines, [O III] and [Ar III] (as well as H α), are spatially concentrated towards the interior of the nebula, contrary to the low excitation lines [N II] and [S II]. Whereas some of these features could be due to the exact positioning of the slit, as the images do not show a brightness difference between both filaments, a noticeable ionization stratification is present within Sab 99.

4 INFRARED EMISSION

The mid-IR emission at 24 μ m revealed by the *Spitzer* MIPS image in Figure 6 is spatially consistent with the optical emission; the mid-IR emission shows two opposite arms, whose curvature mimics that of the optical ones, separated by a dark lane. The two brightest mid-IR clumps are coincident with the two brightest optical knots denoted as L-M and R-S in Figure 4. It is interesting to note that the infrared emission is fully enclosed within the optical boundaries of the PN (bottom panel of Fig. 6, the three IR spots located outside the PN area are actually associated with background stars).

This spatial distribution suggests that the mid-IR emission in the 24 μ m MIPS band could be attributed to the high-excitation [Ne V] λ 24.3 μ m and [O IV] λ 25.9 μ m emission lines rather than to cold

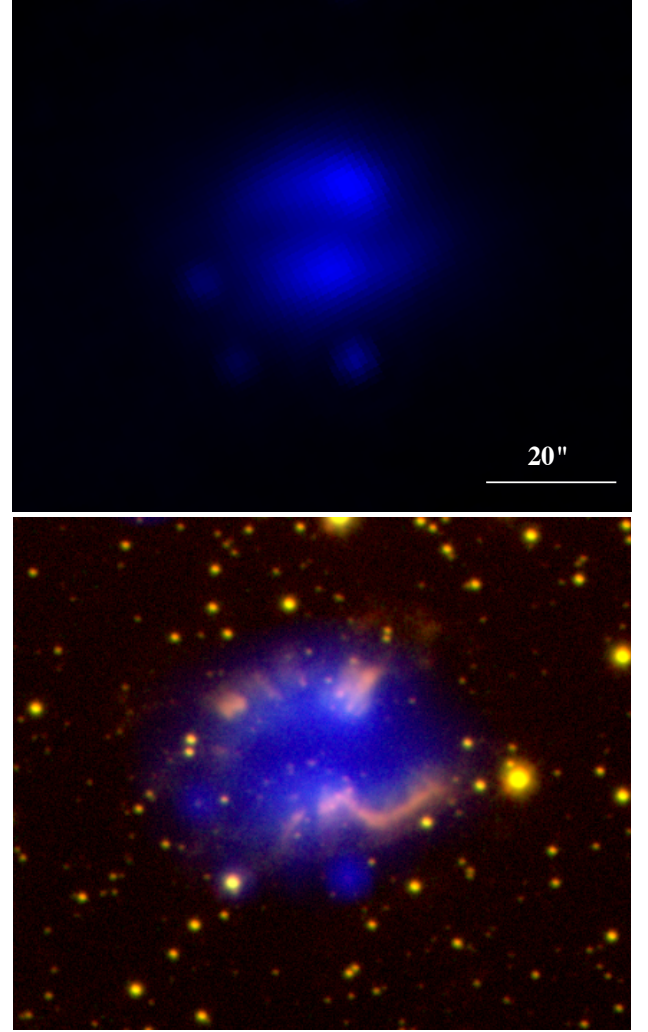


Figure 6. (top) *Spitzer* MIPS 24 μ m band image of Sab 99. The emission shows two hemispheres separated by a dark lane. (bottom) NOT ALFOSC and *Spitzer* MIPS 24 μ m color composite picture of Sab 99 with red, green, and blue corresponding to [N II], H α and the 24 μ m emission. The two optical arms encompass very well the mid-IR emission, while the dark lane is coincident with the optical innermost regions of the nebula. North is top, east to the left.

dust (Chu et al. 2009), but there are no available IR spectra to confirm it.

5 MORPHO-KINEMATIC MODELLING

Using the morphological and kinematical information derived from the high resolution NOT images and high-dispersion MES observations, it is possible to build a spatio-kinematic model of Sab 99 to determine its physical structure. For this purpose we will use the spatio-kinematic code SHAPE (Steffen et al. 2011).

The PV diagrams obtained from slits A and B across the northern arm indicate the presence of a number of knots aligned along a blue-shifted curve, whereas those of slits D and E shows a number of mostly red-shifted knots also along a curve (Fig. 3). The position and velocity of these knots are indicative of a tilted torus. Combined

Table 7. Determination of the electronic temperatures and densities for the brightest knots using the Monte Carlo procedure.

	Region a2		Region b3		Region b4		Region c4	
	Mean	σ	Mean	σ	Mean	σ	Mean	σ
T_e [N II](K)	9570	990	9090	920	10850	1090	8790	650
n_e [S II](cm ⁻³)	280	240	465	350	410	330	350	230

Table 8. Mean ionic and total abundances in logarithmic scale for the individual brightest knots in the upper and lower arms using a Monte Carlo Procedure.

Ion	Region a2		Region b3		Region b4		Region c4	
	N(X)/N(H+)	σ	N(X)/N(H+)	σ	N(X)/N(H+)	σ	N(X)/N(H+)	σ
He ¹⁺	-1.01	0.08	-1.26	0.10	-1.22	0.10	-1.10	0.07
He ²⁺	-1.00	0.13	-1.20	0.14	-1.27	0.16	-1.09	0.10
N ⁰	-4.83	0.27
N ¹⁺	-3.90	0.16	-4.04	0.18	-4.28	0.17	-4.12	0.13
O ⁰	-4.15	0.20	-4.18	0.21	-4.57	0.20	-4.49	0.16
O ¹⁺	-3.41	0.34	-3.35	0.36	-3.83	0.32	-3.49	0.27
O ²⁺	-3.36	0.34	-3.35	0.36	-3.76	0.32	-3.60	0.29
S ¹⁺	-5.59	0.16	-5.59	0.16	-5.85	0.16	-5.62	0.12
S ²⁺	-4.87	0.18
Ar ²⁺	-5.64	0.16	-5.61	0.17	-5.79	0.17	-5.51	0.13
Ne ²⁺	-4.12	0.13
He/H	-0.70	0.10	-0.93	0.12	-0.94	0.12	-0.79	0.08
O/H	-2.88	0.35	-2.82	0.36	-3.31	0.33	-3.04	0.28
N/H	-3.42	0.18	-3.56	0.18	-3.81	0.18	-3.71	0.14
Ar/H	-5.42	0.18	-5.37	0.18	-5.58	0.18	-5.30	0.14
S/H	-5.01	0.16	-5.03	0.17	-5.26	0.16	-5.12	0.13
Ne/H	-3.88	0.15

with the remaining spectra associated to the slits passing through both arms, i.e. slits F, G, and H, we notice some degree of symmetry between opposite knots, suggesting that they are all indeed contained in a truncated torus that contains regions of varying density.

The spatio-kinematic model of Sab 99 is presented in Figure 7. The nebula is mostly composed of a broken torus $\simeq 40''$ in length whose symmetry axis is tilted by $\simeq 40^\circ$ with the plane of the sky. The systemic velocity of the torus would be $v_{\text{LSR}} \approx 10 \text{ km s}^{-1}$. The synthetic PV diagrams produced at the location of the MES slits in Figure 8 provide a satisfactory fit to the observed PV diagrams (Fig. 3), with a number of blue- and red-shifted knots. We note that the faint surface brightness and fragmented appearance of Sab 99 hamper an accurate determination of the inclination, size, and systemic velocity of this torus. Different models with the knots being relatively co-planar within an inclination with the plane of the sky of the torus axis in the range 35° – 45° produce synthetic PV diagrams consistent with those observed. The large variance of the radial velocities of these knots, mostly in the northern arm, suggests a gradual uncoupling from the original structure.

The high-dispersion MES observations did not detect the emission from the structure registered in the much deeper GTC OSIRIS observations along the slit "c" as marked by the labels "c1" and "c6" in Figure 2. Such information is not sufficient to constrain the shape and extent of this structure, which we propose is the pair of bipolar lobes orthogonal to the disrupted torus of Sab 99 illustrated in Figure 7.

6 DISCUSSION

6.1 The true shape of Sab 99

The morphology of Sab 99 could be associated *at first* to the broken edges of an evolved bipolar PN with a pinched waist. The bipolar axis of such a PN seems oriented along the NW to SE direction with PA $\sim -65^\circ$. Sab 99 would be morphologically similar to PNe with pinched waists, such as NGC 2818 (Vázquez 2012), NGC 650-1 (Ramos-Larios et al. 2018) and PNG 321.6+02.2 (Corradi et al. 1997), but the lack of kinematic evidence for a fast outflow along PA -65° seems to question this interpretation.

The deep GTC OSIRIS spectra, however, unveil the presence of two faint clumps located on either side of the main structure along a direction at PA $\sim -10^\circ$. Thus, Sab 99 would actually be a fragmented ring-like structure with the faint remains of a bipolar outflow whose axis is oriented along the NE to SW direction. The detailed orientation and geometry of this outflow and the ring-like structure have been constrained with the kinematic and morphological information using a SHAPE model (see previous section). In this case, Sab 99 would rather compare to objects such as NGC 5189 (Sabin et al. 2012) or NGC 6309 (Vázquez et al. 2008). To some extent we can also consider the morphological similarities with IPHASX J194359.5+170901 (or PN G054.2-03.4, a.k.a. the Necklace Nebula, Corradi et al. 2011), with its well defined ring of knots and remnant of bipolar ejecta.

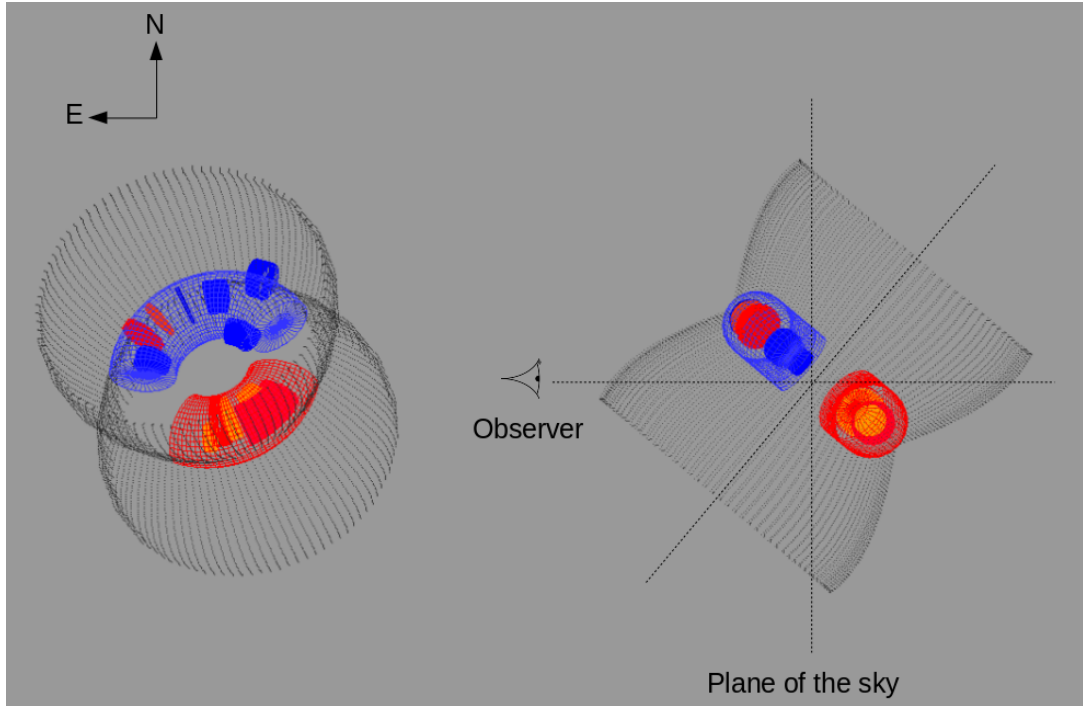


Figure 7. Schematic images of Sab 99 based on our best fit spatio-kinematic SHAPE model projected onto the plane of the sky (left) and rotated by 90° (right). The color code for the knots indicates the blue- and red-shifted components, where an additional orange color in the red-shifted region has been used to distinguish among adjacent knots. The length and morphology of the bipolar outflows are only presented for illustrative purposes.

6.2 A distant and old PN

The distance is a fundamental physical parameters in the study of a PN, but it is also one of the least well determined. The broken morphology of Sab 99 makes uncertain any determination of an average radius, which is a critical datum to determine the distance to a PN using the statistical method based on the relationship between the $H\alpha$ surface brightness ($S_{H\alpha}$) and the radius of a PN (Frew et al. 2016). Alternatively, the distance can be derived from the extinction to the PN if the relationship between the extinction and the distance along the line of sight is known.

Since the extinction derived at different locations of the nebula is relatively constant, we can assume that the circumstellar extinction is negligible.

Detailed 3D extinction maps for the Northern Galactic plane have been generated using photometric data obtained in the framework of IPHAS (Sale et al. 2014). This extinction-distance method was applied by Giammanco et al. (2011) to a sample of known PNe using earlier versions of those extinction maps and concluded that distances could be obtained with an accuracy better than 35% depending on the uncertainty on the determination of the nebular extinction and on the quality of the extinction map along this exact line of sight. The authors also described the main sources of error associated with the method. As for Sab 99, we will adopt the 3D extinction map centered at $l = 056.125^\circ$, $b = -00.542^\circ$ (Fig. 9). The mean $c(H\beta)$ value of 2.14 ± 0.15 derived in previous sections implies an extinction $A_V = 4.6 \pm 0.3$ that intersects the extinction to distance curve in Figure 9 at a distance of $7.1^{+0.8}_{-0.3}$ kpc.

The main caveat in this distance estimation is that the source is centered at ≈ 7.8 from the center of the $10' \times 10'$ map and the variation on the extinction might play an important role. We examined

other adjacent maps⁴ and found the closest one with trustworthy results on the distance for the value of A_V previously derived to be centered at $l = 056.125^\circ$, $b = -00.375^\circ$. It indicates a distance of $6.3^{+0.5}_{-0.9}$ kpc for Sab 99, thus the distance of 7.1 kpc can be considered as an upper limit taking into account variations on the visual extinction along the line of sight.

The velocity distribution indicates the overall motion of the central nebula with the northern section of the ring being mostly blue-shifted and the southern counterpart being red-shifted. The values of the radial velocities are moderate, with a maximum of 30.1 km s^{-1} . Taking into account the geometry obtained with our SHAPE model, where the central filamentary structure is an expanding torus following an homologous law, a mean expansion velocity of $25 \pm 5 \text{ km s}^{-1}$ and a mean radius of $19'' \pm 10''$ can be estimated.

At a distance of 7.1 kpc, this results in a radius of $0.65^{+0.42}_{-0.37}$ pc and a kinematical age $\lesssim 26000$ yr.

Although the latter value is highly affected by the large uncertainties in distance, ring radius and expansion velocity, and depends on the strong assumption of an expansion at constant speed, a relatively late evolutionary stage is consistent with the fragmented and diffuse appearance of Sab 99.

6.3 Estimated physical and chemical characteristics

The high excitation [O III] $\lambda 4363\text{\AA}$, [Cl III] or [Ar IV] emission lines are absent from our spectra and most of the calculations referring to the physical parameters and abundances were performed using low excitation ions. The physical analysis reveals a relatively homogeneous nebular temperature (within the error bars) with $\langle T_e [\text{N II}] \rangle$

⁴ <http://www.iphas.org/extinction/>

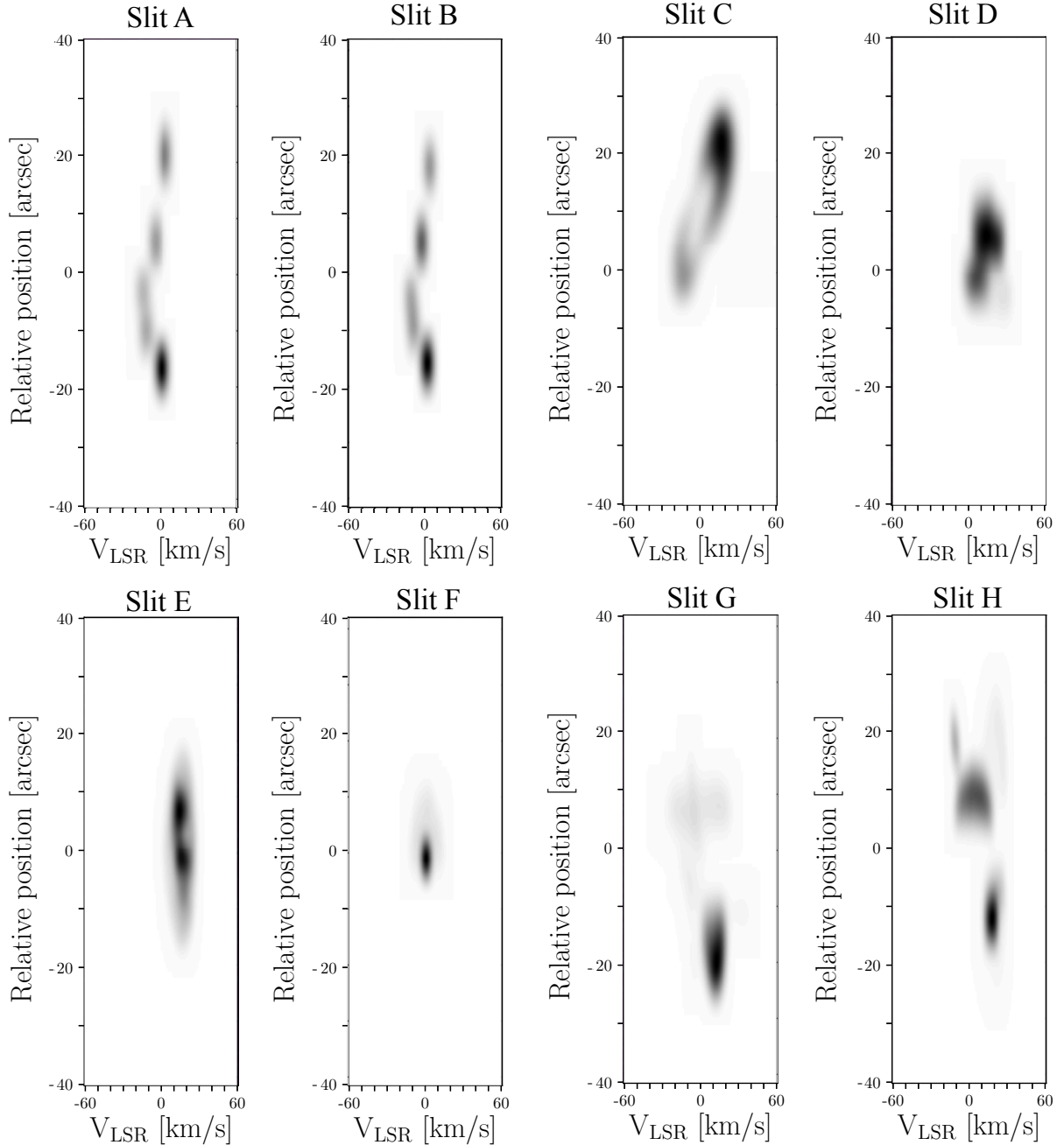


Figure 8. Synthetic PV diagrams of the echellograms shown Figure 3 obtained from the best fit spatio-kinematic SHAPE model shown in Figure 7.

≈ 9600 K and low density $\langle n_e [\text{S II}] \rangle \approx 380 \text{ cm}^{-3}$. A comparison with the much younger PN NGC 6309, with structures aged between 3700 and 4000 years, indicates roughly similar temperatures ($T_e [\text{N II}] = 10200\text{--}11800$ K), but much higher densities ($n_e [\text{S II}] = 1600\text{--}3800 \text{ cm}^{-3}$) in the central knotty torus (Vázquez et al. 2008). The brightest knots in Sab 99 are particularly rich in He, N and O (Table 8). The average $\langle \text{N/O} \rangle$ value of ≈ 0.235 and average $\langle \text{He/H} \rangle$ value of ≈ 0.148 can be used to establish the nature of the PN. Hence, based on these abundance ratios and Kingsburgh & Barlow (1994)’s definition, Sab 99 is a non-Type I PNe as $\text{N/O} \leq 0.8$ although we note that the He/H abundance is large and more typical of a Type I. In addition, the Peimbert (1978) classification scheme identifies the PN as a Type II based on the same N/O ratio. Sab 99

can be considered as a relatively high excitation nebula as indicated by the presence of the He II $\lambda 4686\text{\AA}$ emission line (with $I/\text{H}\beta$ up to 105 ± 25 in the Region c and averaging 65 ± 12 in the whole nebula) and a mostly oxygen-rich nebula.

Therefore, Sab 99 is likely to have an intermediate mass in the $\approx 1.2\text{--}2.0 M_\odot$ range. The evolutionary models of Marigo (2001) can be used to provide some constraints on the progenitor initial mass (M_i) based on the mean He/H, $\log (\text{N/H})$ and $\log (\text{O/H})$ of Sab 99. This results in an initial mass estimate $\approx 2\text{--}3 M_\odot$ for a metallicity $0.019 Z_\odot$ i.e. the upper range limit for this intermediate mass PN. Following the method by Maciel et al. (2010) using the N/O abundance ratio, the central star mass (M_{CSPN}) is estimated to be $\sim 0.61 M_\odot$.

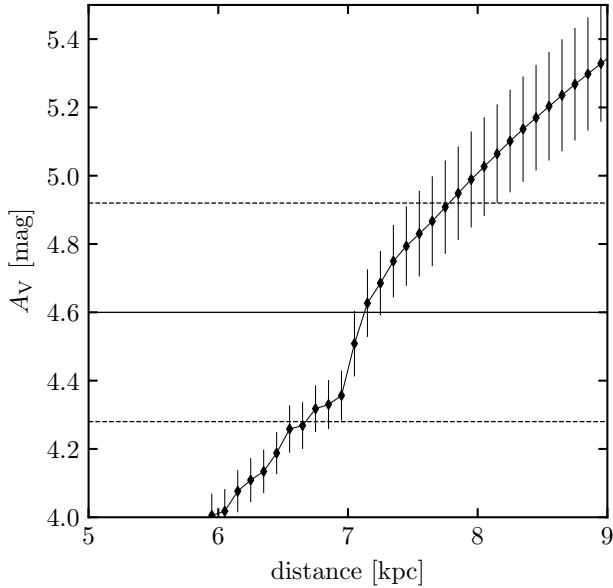


Figure 9. Distance-extinction relationship derived from an extinction map close to the line of sight of Sab 99. Only the portion of the curve with the largest slope where it is possible to derive distance is shown. The extinction of Sab 99 is denoted by a horizontal solid line at $A_V = 4.6$ mag, with the horizontal dotted lines marking the 1σ uncertainties.

We conducted a simple CLOUDY (Ferland et al. 2017) photoionisation modelling for a nebula with the physical structure of the central ring described by our SHAPE model and the chemical abundances as those listed in Table 8. A model atmosphere by Rauch (2003) was adopted to describe the emission from the central star. The best fit models for the low and high excitation emission lines imply an effective temperature $\log(T_{\text{eff}}) \approx 5-5.2$ and luminosities in the range $\log(L/L_{\odot}) \approx 3.5-4$. From the models, and assuming the reddening $A_V = 4.6 \pm 0.3$, we estimated that the visual magnitude of the central star is fainter than $\sim 21-22$ mag. This is in concordance with the magnitudes of the field's stars detected in the central area of Sab 99 showing r' mag fainter than ~ 20 (Barentsen et al. 2014). Again, the errors on the different parameters involved have to be taken into account, but the results tend to support the fact that the central star is not visible.

The high effective temperature of the central star of Sab 99 and the detailed spatial distribution of the emission in the *Spitzer* MIPS $24 \mu\text{m}$ band (Fig. 6) provides additional support to the origin of this emission from the [O IV] line at $25.9 \mu\text{m}$ (Chu et al. 2009).

We would therefore be detecting emission lines from highly ionized material inside the spatial boundaries of the optical emission and indeed the CLOUDY model described above implies a flux for this line 8 times that of the $H\beta$ line. Whereas dust may still be present inside the nebula, we note that there are no variations (within the errors) of $c(H\beta)$ across the nebula, suggesting a homogeneous dust distribution. Mid-IR spectroscopic observations are required to fully settle down this issue.

7 CONCLUSIONS

We have presented a detailed study of the spatial, kinematic, spectroscopic, and chemical properties of the newly discovered IPHAS PN

Sab 99 based on sub-arcsec optical narrow-band images and high-dispersion echelle and deep optical intermediate-dispersion spectra. This investigation has allowed us to achieve sound conclusions on different aspects of this source.

The physical structure of Sab 99 is bipolar, but, contrary to naive expectations based on its optical morphology, the two opposite arm-like structures are fragmented remains of an equatorial torus aligned along the East-West direction, with an extremely faint bipolar outflow along the North-South direction detected in deep GTC OSIRIS spectra that escapes detection in our NOT ALFOSC optical narrow-band images. Deeper images in the [N II] emission could provide information on its detailed morphology and extent. The kinematics of individual knots in this torus indicates their gradual uncoupling and destruction of this structure.

The progenitor star of Sab 99 had an initial mass of $\approx 2-3 M_{\odot}$, as implied by the comparison of the chemical abundances of the nebula, typical of a Type II PN, with the expectations of models of chemical evolution of low- and intermediate-mass stars. The mass of the stellar remnant is also significant, $\sim 0.61 M_{\odot}$. According to simple CLOUDY photoionization models, the central star has nowadays a high effective temperature, around 10^5 K, resulting in notable nebular emission in the high excitation lines of He II $\lambda 4686 \text{ \AA}$ and perhaps [O IV] $25.9 \mu\text{m}$.

The nebula is assumed at a distance of $7.1^{+0.8}_{-0.3}$ kpc, obtained with the IPHAS extinction maps and owing the variations of interstellar extinction in the line of sight. This in turns implies a kinematic age $\lesssim 26000$ yr. Although this figure is affected by large uncertainties, a late evolutionary stage for Sab 99 would be consistent with the low density and disrupted morphology and kinematics of its equatorial ring, as well as the high effective temperature of its central star.

Although Sab 99 is inherently faint and complex, our investigation has been able to conclude that it was once a bipolar PN of which only a disrupted equatorial ring remains, while the bipolar lobes are no longer visible, except for some remaining patches. The torus at the nebular equator is still present but shows spatial and kinematic signs of a gradual dismantlement. Its central star has a high effective temperature. Such evolved object is one kind of PNe that can be expected to be found in IPHAS.

ACKNOWLEDGMENTS

The authors are thankful to the referees for their comments that improved the present paper. LS acknowledges support from PAPIIT grant IN-101819 (Mexico). MAG acknowledges support from grant AYA PGC2018-102184-B-I00 co-funded with FEDER funds. SZ works under the collaboration agreement "UNAM-TecNM 43310-3020-30-IX-15". JAT and MAG are funded by UNAM DGAPA PAPIIT project IA100720. GRL acknowledges support from CONA-CyT (grant 263373) and PRODEP (Mexico).

This work is partially based on observations collected at the Observatorio Astronómico Nacional at San Pedro Mártir, B.C., Mexico and we thank the daytime and night support staff at the OAN-SPM for facilitating and helping obtain our observations. Based on observations made with the Nordic Optical Telescope, operated by the Nordic Optical Telescope Scientific Association, and the Gran Telescopio Canarias (GTC), both installed in the Spanish Observatorio del Roque de los Muchachos of the Instituto de Astrofísica de Canarias in La Palma, Spain. This paper makes use of data obtained as part of the INT Photometric $H\alpha$ Survey of the Northern Galactic Plane (IPHAS, www.iphas.org) carried out at the Isaac Newton Telescope (INT). The INT is operated on the island of

La Palma by the Isaac Newton Group in the Spanish Observatorio del Roque de los Muchachos of the Instituto de Astrofísica de Canarias. All IPHAS data are processed by the Cambridge Astronomical Survey Unit, at the Institute of Astronomy in Cambridge. The bandmerged DR2 catalogue was assembled at the Centre for Astrophysics Research, University of Hertfordshire, supported by STFC grant ST/J001333/1. The OSN director is acknowledged for awarding observations through a DDT program and the telescope operator Alfredo Sota for conducting the observations. This work is based in part on observations made with the *Spitzer* Space Telescope, which is operated by the Jet Propulsion Laboratory, California Institute of Technology under a contract with NASA. In memoriam of Johannes Andersen, director of the NOT from 2002 to 2013.

DATA AVAILABILITY

The data underlying this article will be shared on reasonable request to the corresponding author.

REFERENCES

- Akras S., Guzman-Ramirez L., Gonçalves D. R., 2019, *MNRAS*, 488, 3238
- Asensio Ramos A., Martínez González M. J., Manso Sainz R., Corradi R. L. M., Leone F., 2014, *ApJ*, 787, 111
- Balick B., Frank A., 2002, *ARAA*, 40, 439
- Balick B., Frank A., Liu B., Corradi R., 2018, *ApJ*, 853, 168
- Barentsen G., Farnhill H. J., Drew J. E., González-Solares E. A., Greimel R., Irwin M. J., Miszalski B., Ruhland C., et al. 2014, *ArXiv e-prints*
- Cardelli J. A., Clayton G. C., Mathis J. S., 1989, *ApJ*, 345, 245
- Chu Y.-H., Gruendl R. A., Guerrero M. A., Su K. Y. L., Bilikova J., Cohen M., Parker Q. A., Volk K., Caulet A., Chen W.-P., Hora J. L., Rauch T., 2009, *ApJ*, 138, 691
- Corradi R. L. M., García-Rojas J., Jones D., Rodríguez-Gil P., 2015, *ApJ*, 803, 99
- Corradi R. L. M., Sabin L., Miszalski B., Rodríguez-Gil P., Santander-García M., Jones D., Drew J. E., Mampaso A., Barlow M. J., Rubio-Díez M. M., Casares J., Viironen K., Frew D. J., Giammanco C., Greimel R., Sale S. E., 2011, *MNRAS*, 410, 1349
- Corradi R. L. M., Schwarz H. E., 1995, *A&A*, 293, 871
- Corradi R. L. M., Villaver E., Mampaso A., Perinotto M., 1997, *A&A*, 324, 276
- Delgado-Inglada G., Morisset C., Stasińska G., 2014, *MNRAS*, 440, 536
- Drew J. E., Greimel R., Irwin M. J., Aungwerojwit A., Barlow M. J., Corradi R. L. M., Drake J. J., Gänsicke B. T., et al., 2005, *MNRAS*, 362, 753
- Ferland G. J., Chatzikos M., Guzmán F., Lykins M. L., van Hoof P. A. M., Williams R. J. R., Abel N. P., Badnell N. R., Keenan F. P., Porter R. L., Stancil P. C., 2017, *Rev. Mex. Astron. Astrofis.*, 53, 385
- Filippenko A. V., 1982, *PASP*, 94, 715
- Frew D. J., Parker Q. A., Bojičić I. S., 2016, *MNRAS*, 455, 1459
- García-Díaz M. T., Steffen W., Henney W. J., López J. A., García-López F., González-Buitrago D., Áviles A., 2018, *MNRAS*, 479, 3909
- Giammanco C., Sale S. E., Corradi R. L. M., Barlow M. J., Viironen K., Sabin L., Santander-García M., Frew D. J., Greimel R., Miszalski B., Philipps S., Zijlstra A. A., Mampaso A., Drew J. E., Parker Q. A., Napiwotzki R., 2011, *A&A*, 525, A58
- González-Solares E. A., Walton N. A., Greimel R., Drew J. E., Irwin M. J., Sale S. E., Andrews K., Aungwerojwit A., Barlow M. J., van den Beselaar E., Corradi R. L. M., Gänsicke B. T., et al., 2008, *MNRAS*, 388, 89
- Groot P. J., Verbeek K., Greimel R., Irwin M., González-Solares E., Gänsicke B. T., de Groot E., Drew J., et al. 2009, *MNRAS*, 399, 323
- Hillwig T. C., Jones D., De Marco O., Bond H. E., Margheim S., Frew D., 2016, *ApJ*, 832, 125
- Huarte-Espinosa M., Frank A., Balick B., Blackman E. G., De Marco O., Kastner J. H., Sahai R., 2012, *MNRAS*, 424, 2055
- Jones D., Boffin H. M. J., 2017, *Nature Astronomy*, 1, 0117
- Jones D., Wesson R., García-Rojas J., Corradi R. L. M., Boffin H. M. J., 2016, *MNRAS*, 455, 3263
- Kingsburgh R. L., Barlow M. J., 1994, *MNRAS*, 271, 257
- López J. A., García-Díaz M. T., Steffen W., Riesgo H., Richer M. G., 2012, *ApJ*, 750, 131
- Luridiana V., Morisset C., Shaw R. A., 2015, *A&A*, 573, A42
- Maciel W. J., Costa R. D. D., Idiart T. E. P., 2010, *A&A*, 512, A19
- Marigo P., 2001, *A&A*, 370, 194
- Meaburn J., López J. A., Gutiérrez L., Quiróz F., Murillo J. M., Valdéz J., Pedrayes M., 2003, *Rev. Mex. Astron. Astrofis.*, 39, 185
- Peimbert M., 1978, in Terzian Y., ed., *Planetary Nebulae Vol. 76 of IAU Symposium, Chemical abundances in planetary nebulae.*, pp 215–224
- Ramos-Larios G., Guerrero M. A., Nigoche-Netro A., Olguín L., Gómez-Muñoz M. A., Sabin L., Vázquez R., Akas S., Ramírez Vélez J. C., Chávez M., 2018, *MNRAS*, 475, 932
- Rauch T., 2003, *A&A*, 403, 709
- Rieke G. H., Young E. T., Engelbracht C. W., Kelly D. M., Low F. J., Haller E. E., Beeman J. W., Gordon K. D., Stansberry J. A., Misselt K. A., Cadien J., Morrison J. E., Rivlis G., Latter W. B. e. a., 2004, *ApJs*, 154, 25
- Sabin L., Gómez-Muñoz M. A., Guerrero M. A., Zavala S., Ramos-Larios G., Vázquez R., Corral L., Blanco Cárdenas M. W., Guillén P. F., Olguín L., Morisset C., Navarro S., 2017, *MNRAS*, 467, 3056
- Sabin L., Parker Q. A., Corradi R. L. M., Guzman-Ramirez L., Morris R. A. H., Zijlstra A. A., et al., 2014, *MNRAS*, 443, 3388
- Sabin L., Vázquez R., López J. A., García-Díaz M. T., Ramos-Larios G., 2012, *Rev. Mex. Astron. Astrofis.*, 48, 165
- Sahai R., Villar III G. G., Morris M., 2011, in *Asymmetric Planetary Nebulae 5 Conference Young planetary nebulae: Hubble Space Telescope imaging and new morphological classifications system*
- Sale S. E., Drew J. E., Barentsen G., Farnhill H. J., Raddi R., Barlow M. J., Eisloffel J., Vink J. S., Rodríguez-Gil P., Wright N. J., 2014, *MNRAS*, 443, 2907
- Steffen W., Koning N., Wenger S., Morisset C., Magnor M., 2011, *IEEE Transactions on Visualization and Computer Graphics*, Volume 17, Issue 4, p.454-465, 17, 454
- Tocknell J., De Marco O., Wardle M., 2014, *MNRAS*, 439, 2014
- Tody D., 1986, in Crawford D. L., ed., *Proc. SPIE Vol. 627 of Society of Photo-Optical Instrumentation Engineers (SPIE) Conference Series, The IRAF Data Reduction and Analysis System.* p. 733
- Vázquez R., 2012, *ApJ*, 751, 116
- Vázquez R., Miranda L. F., Olguín L., Ayala S., Torrelles J. M., Contreras M. E., Guillén P. F., 2008, *A&A*, 481, 107
- Viironen K., Greimel R., Corradi R. L. M., Mampaso A., Rodríguez M., Sabin L., Delgado-Inglada G., Drew J. E., et al. 2009, *A&A*, 504, 291
- Wesson R., Jones D., García-Rojas J., Boffin H. M. J., Corradi R. L. M., 2018, *MNRAS*, 480, 4589

This paper has been typeset from a \LaTeX file prepared by the author.